Structured Beamforming Based on Orbital Angular Momentum Mode-Group

Xianmin Zhang, Shilie Zheng, *Member, IEEE*, Xiaowen Xiong, *Member, IEEE*, Zelin Zhu, Yuqi Chen, *Graduate Student Member, IEEE*, Zhixia Wang, Xiaonan Hui, Wei E. I. Sha, *Senior Member, IEEE*, and Xianbin Yu, *Senior Member, IEEE*

(Invited Paper)

***Abstract*—The structured beams, which can manipulate arbitrary intensity and phase of electromagnetic rays, are significant in communication and sensing. The vortex electromagnetic wave carrying orbital angular momentum (OAM) exhibits the phase distribution of the helical wavefront, which can be viewed as a complete set of eigenmodes for electromagnetic waves. It provides a flexible beamforming method to achieve the azimuthal pattern diversity by the spatial superposition of multiple specific OAM modes. We have proposed a novel form of OAM wave with a two-dimensional structure called plane spiral OAM (PS-OAM), which is conducive to overlapping different modes. Based on this, the PS-OAM mode-group can be employed to modify the spatial beam structure and form structured electromagnetic beams. This kind of beam not only retains the inherent vorticity and orthogonality of the OAM waves but also tackles the difficulties in applications stemming from the singularity-caused dark zone and beam divergence of conventional OAM waves. In this paper, the construction and manipulation of the structured beams are investigated, and the properties are analyzed. The potential applications in multiple-input multiple-output (MIMO) communication, orthogonal multiplexing communication, and spatial field digital modulation (SFDM) communication are envisioned.**

***Index Terms*—Structured radio beam, orbital angular momentum, plane spiral OAM, MIMO communication, space division multiplexing, spatial field digital modulation.**

I. Introduction

ORBITAL angular momentum (OAM) is the essential physical parameter of the electromagnetic wave manifesting the rotational symmetry of the electromagnetic field, which is an extrinsic property describing the phase singularity and the beam vorticity. OAM was first found in the optical domain [1], and the applications based on OAM have ranged from optical manipulation to high-capacity communications [2]. Over the last decade, it was found that the photon OAM is not restricted to the optical domain and can be used in the terahertz to microwave domain [3], [4].

In recent times, structured light has become synonymous with OAM. The richness of the topic, as well as its myriad of applications, has attracted much attention. The superposition of composite optical vortex has already been proposed to constitute the structured beams, which are indeed emerging as a new frontier in modern photonics [5]. In the same way, structured radio beams with diverse radiation patterns exhibit colossal potential in many applications. However, the divergence of conventional OAM beam scales approximately with the square root of the mode number $|l|$ [6], indicating that the radio waves carrying different OAM modes might have different divergence angles. These features make it difficult to overlap the mainlobes of multiple OAM-carrying waves, which results in many challenges for structured beamforming based on OAM in the radio frequency regions.

We have proposed a novel form of OAM radio wave, termed plane spiral OAM (PS-OAM) electromagnetic wave, to tackle the difficulties stemming from the singularity-caused dark zone and beam divergence [7], [8]. Fig. 1(a) shows the schematic of the PS-OAM wave, for comparison, the conventional OAM wave is also shown in Fig. 1(b). Instead of propagating along the main axis with the helical phase fronts in the three-dimensional

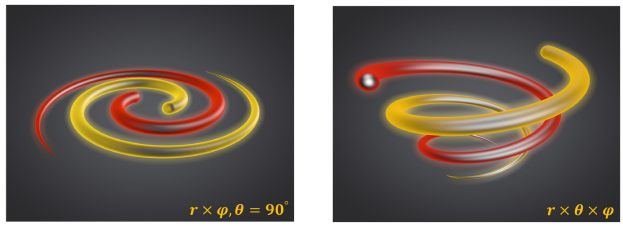

(a) (b)

Fig. 1. The schematic of OAM waves. (a) Plane spiral OAM (PS-OAM) wave, and (b) general OAM wave.

Manuscript received 31 August 2022; revised 12 October 2022; accepted 13 October 2022. Date of publication 17 October 2022; date of current version 3 April 2023. This work was supported by the National Natural Science Foundation of China under Grants 62171409 and 61571391. *(Corresponding author: Xianmin Zhang.)*

Xianmin Zhang is with the College of Information Science and Electronic Engineering, Zhejiang University, Hangzhou 310027, China, and also with the School of Information Science and Engineering, NingboTech University, Ningbo 315100, China (e-mail: zhangxm@zju.edu.cn).

Shilie Zheng, Xiaowen Xiong, Zelin Zhu, Yuqi Chen, Zhixia Wang, and Wei E. I. Sha are with the College of Information Science and Electronic Engineering, Zhejiang University, Hangzhou 310027, China (e-mail: zhengsl@zju.edu.cn; xiongxiaowen@zju.edu.cn; zelinzhu@zju.edu.cn; chen_yuqi@zju.edu.cn; wangzhixia@zju.edu.cn; weisha@zju.edu.cn).

Xiaonan Hui and Xianbin Yu are with the College of Information Science and Electronic Engineering, Zhejiang University, Hangzhou 310027, China, and also with the Zhejiang Lab, Hangzhou 311121, China (e-mail: x.hui@zju.edu.cn; xyu@zju.edu.cn).

Color versions of one or more figures in this article are available at https://doi.org/10.1109/JLT.2022.3215211.

Digital Object Identifier 10.1109/JLT.2022.3215211

space ($\rho \times \theta \times \varphi$ in spherical coordinates) as the conventional OAM wave, the PS-OAM wave propagates mainly along the transverse direction with a two-dimensional structure ($\rho \times \varphi$, $\theta = 90°$) and spiral phase distribution in the radial plane. There is no singularity along the propagating path, and all PS-OAM modes have the same radiation pattern with linearly polarized in the far field region. Thus the overlapping of different OAM modes can be easily achieved. It will significantly benefit the mode grouping and multi-beam synthesis.

The mode-group superposed by specific single-mode PS-OAM waves has been proved to be a flexible beamforming method to achieve the azimuthal pattern diversity [9]. Since the PS-OAM waves with the same propagation direction constitute a complete set of eigenmodes, with a particular strategy to select several PS-OAM modes and superposing them into a mode-group, a reconfigurable beamforming scheme could be achieved by manipulating the intensity and the initial phase of each PS-OAM mode among the group. The structured beam not only retains the inherent vorticity and orthogonality of the conventional OAM wave but also can realize a high gain.

The rest of the paper is organized as follows. Firstly, the beamforming for the structured beams based on PS-OAM is analyzed, and the essential characteristics are discussed. Then, the antenna for the structured radio beam is investigated. Finally, the potential applications of the structured radio beams for multiple-input multiple-output (MIMO) system, orthogonal multiplexing communication, and spatial field digital modulation (SFDM) are explored.

II. Beamforming Based on PS-OAM

Periodic complex exponentials play a central role in treating signals and systems because they can serve as extremely useful building blocks for many other signals. In the spatial domain, OAM waves possess an azimuthal phase distribution of $\exp(-\mathrm{j}l\varphi)$. The azimuthal angle φ is periodically linked with the OAM mode number l by Fourier transform. Thus, the transverse far-field radiation pattern of a structured radio beam in the azimuthal domain can be constructed in terms of spiral harmonics, i.e., a beam with arbitrary angular intensity and phase distributions can be obtained by superposed PS-OAM modes.

A. Pencil Beam

This highly directional beam with a single mainlobe is somewhat like sinc function, thus can easily be achieved by superposing many PS-OAM modes with consecutive modes. Supposing there are N PS-OAM modes with a constant mode interval Δl, then the constructed beam can be described as

$$\Phi(\varphi) = \sum_{n=0}^{N-1} A_n \mathrm{e}^{-\mathrm{j}[(l_0+n\Delta l)\varphi+\varphi_n]} \tag{1}$$

where A_n, $l_0 + n\Delta l$, φ_n are the amplitude, the OAM mode number, and the initial phase of the nth PS-OAM mode among the mode-group, respectively. For simplicity, let the weight of each PS-OAM be equal and all the initial phases are 0, the pattern function can be expressed as [10]

$$\Phi(\varphi) = \frac{\sin(\frac{N\cdot\Delta l}{2}\varphi)}{\sin(\frac{\Delta l}{2}\varphi)} \cdot \mathrm{e}^{-\mathrm{j}[l_0+\frac{(N-1)\cdot\Delta l}{2}]\varphi} \tag{2}$$

where l_0 is the first OAM mode among the superposed PS-OAM waves.

$\sin(N \cdot \Delta l/2 \cdot \varphi)/\sin(\Delta l/2 \cdot \varphi)$ is the amplitude factor, which is dependent on N and Δl. It describes the directional gain of the constructed radio beam, which provides an efficient solution to generate high-gain beams. Fig. 2 shows the normalized beam patterns at the transverse plane by grouping 2, 8, and 16 consecutive PS-OAM waves, respectively. The mainlobe becomes narrower, and the number of the sidelobes increases with the increasing components of PS-OAM waves. It shows clearly that a highly oriented beam can be synthesized when many more PS-OAM modes are combined. The weight of each PS-OAM can be complex, including the amplitude and phase, and the OAM modes can be arbitrary orders.

Multi-beam synthesis can also be easily obtained using the superposition of the PS-OAM waves. Fig. 3 shows the various angular intensity patterns by (2). The number of the superposed PS-OAM waves $N = 8$. Fig. 3(a)–(c) correspond to $l_0 = 1$, while $\Delta l =$ 1, 2 and 3, respectively. It can be seen that the interval of the superposed OAM mode Δl determines the number of the mainlobes. $\Delta l = 1$ corresponds to one mainlobe, $\Delta l = 2$ corresponds to two mainlobes, and so on. If a large OAM mode interval is adopted, multiple mainlobes are easily obtained.

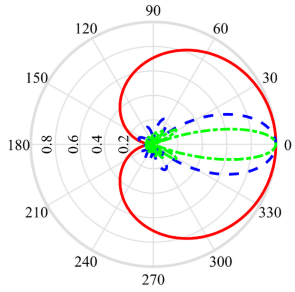

Fig. 2. Normalized beam pattern for 4 PS-OAM modes of $l = \{1, 2\}$ (red line), 8 PS-OAM modes of $l = \{1, 2, 3, \ldots, 8\}$ (blue line), and 16 PS-OAM modes of $l = \{1, 2, 3, \ldots, 16\}$ (green line).

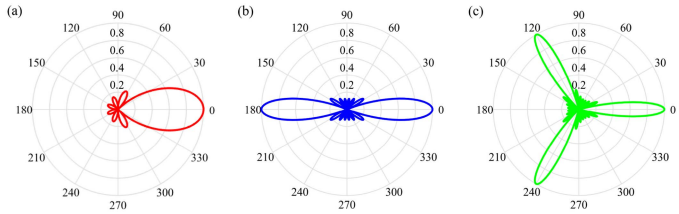

Fig. 3. The angular intensity distribution of 8 PS-OAM waves with different OAM modes at the transverse plane. (a) PS-OAM modes of $l = \{1, 2, 3, 4, 5, 6, 7, 8\}$; (b) PS-OAM modes of $l = \{1, 3, 5, 7, 9, 11, 13, 15\}$; (c) PS-OAM modes of $l = \{1, 4, 7, 10, 13, 16, 19, 22\}$.

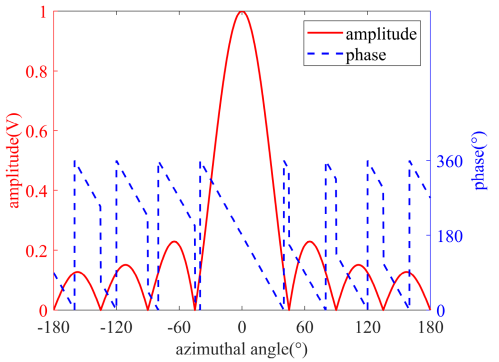

Fig. 4. Normalized amplitude and phase distribution for 8 PS-OAM modes of $l = \{1, 2, 3, 4, 5, 6, 7, 8\}$.

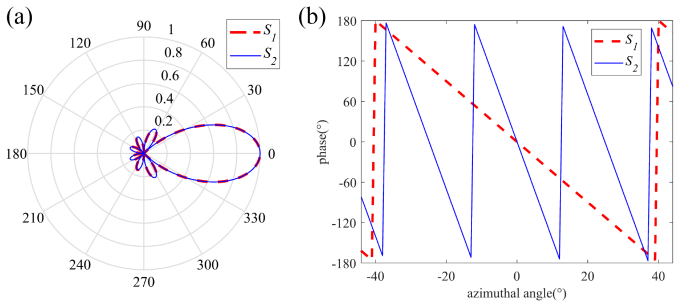

Fig. 5. Structured radio beams with 8 PS-OAM modes. (a) Normalized beam pattern, and (b) the phase distribution within the mainlobe. $S_1 = \{1, 2, 3, 4, 5, 6, 7, 8\}$ (red dash line), $S_2 = \{11, 12, 13, 14, 15, 16, 17, 18\}$ (blue solid line).

B. Vorticity and Orthogonality

The vorticity and orthogonality are the two essential characteristics of vortex waves. The structured beams retain the inherent vorticity and orthogonality of the conventional OAM waves.

As indicated by (2), $\exp\{-\mathrm{j}[l_0 + (N-1)\cdot\Delta l/2]\varphi\}$ is the phase factor depending on l_0, N, and Δl. Interestingly, the phase of the superposed beam changes linearly along the azimuthal angle, and the slope is the average of all the superposed OAM modes which was defined as the equivalent OAM order l_e in [11]. This means that the superposed beam retains the vorticity, and the azimuthal phase distribution can be adjusted by the superposed PS-OAM modes. Since equivalent OAM order $l_e = l_0 + (N-1)\cdot\Delta l/2$, the phase characteristics of the constructed radio beams can be manipulated by selecting the appropriate OAM mode l_0 and mode interval Δl.

Fig. 4 shows the normalized amplitude and phase distribution of the structured radio beam superposed by PS-OAM waves with modes $\{1, 2, 3, 4, 5, 6, 7, 8\}$. Phase is linearly distributed along the azimuthal angle, and the slope of 4.5 exactly matches the average of superposed OAM modes.

According to (1), there can be many PS-OAM groups to form one specific angular intensity pattern. Although the intensity pattern is the same for these beams, their phase characteristics are different. One example is in Fig. 5, which shows the phase distributions of two beams formed by two OAM mode groups. Mode group S_1 is the superposition of modes of $\{1, 2, 3, 4, 5, 6, 7, 8\}$, and mode group S_2 is the superposition of the PS-OAM modes of $\{11, 12, 13, 14, 15, 16, 17, 18\}$. It can be seen that these two OAM groups possess different phase change periods. Moreover, such beams with the same radiation pattern are orthogonal as long as the superposed OAM modes are not overlapped. As we know that more PS-OAM modes superposition results in a narrow mainlobe, it can say that the hybrid wave of group S_1 is approximately orthogonal to that of group S_2 within the mainlobe region. Taking the two OAM groups in Fig. 5 as an example, the correlation coefficient between them is 0 within the 2π aperture while 0.0095 within the mainlobe.

C. Beam Scanning

For the OAM grouping of PS-OAM waves, both the intensity and the phase of the RF beams can adeptly be manipulated. If the superposed PS-OAM waves have regular initial phases, i.e., $\varphi_n = l_n \cdot \Delta\varphi$, then (2) can be expressed as

$$\Phi(\varphi + \Delta\varphi) = \sum_{n=0}^{N-1} A_n \mathrm{e}^{-\mathrm{j}(l_n\varphi + \varphi_n)} = \sum_{n=0}^{N-1} A_n \mathrm{e}^{-\mathrm{j}l_n(\varphi + \Delta\varphi)} \tag{3}$$

As can be seen from (3), the initial phase difference between adjacent modes $\Delta\varphi$ determines the directivity of the structured beam. If the pattern wants to be rotated by $\Delta\varphi$, the phase shift of the feeding port for corresponding PS-OAM wave is $l_n\Delta\varphi$. When the phase shift of each feeding port is regularly controlled, the intensity pattern can be rotated to realize the beam scanning.

There are two interesting aspects here when compared with the generally used beam scanning schemes. One is that using this beam scanning technique, the beam pattern of the constructed wave $\Phi(\varphi + \Delta\varphi)$ remains constant while the whole pattern rotates $\Delta\varphi$ along the azimuthal direction, which is difficult to achieve in phased array systems. The other is that it is the phase shift instead of the time delay that allows the realization of beam scanning, which presents an easy solution for wideband applications.

III. Antennas for Structured Beamforming

A traveling-wave circular slot antenna based on the resonant ring cavity can generate a single mode OAM wave when a 90° hybrid coupler is used to excite the antenna and the phase changes along a circle of $2\pi l$ in the cavity [12], [13]. The amplitude distribution of OAM wave with mode number l in the elevation direction satisfies,

$$A(\theta) \propto J_l[ka\sin(\theta)] \tag{4}$$

where k is the wave number, and a is the radius of the traveling-wave circular slot. The radiation direction can be calculated by (4). A prominent feature of PS-OAM is that the radiation direction is along the transverse plane regardless of the mode number l. There are three ways to help the radiation concentrate on the radial plane.

The first method is to reduce the radius a of the resonant ring cavity. When $ka\sin(\theta)$ is less than the first maximum point of

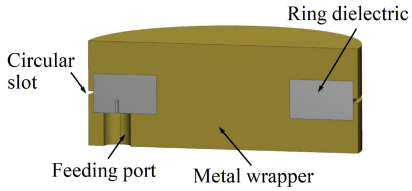

Fig. 6. The section view of the ring dielectric resonator antenna.

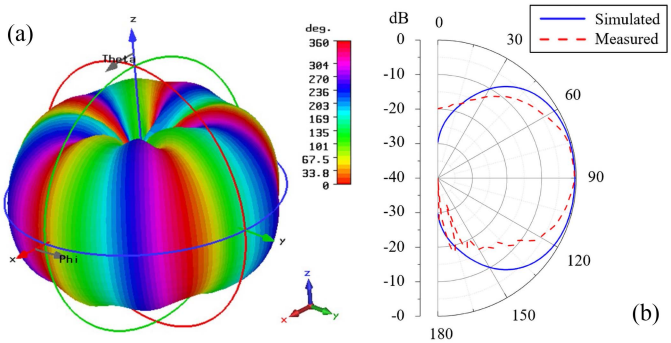

Fig. 7. Electric far-field radiation patterns of the ring dielectric resonator antenna. (a) The simulated 3D pattern, and (b) the simulated (blue solid line) and measured results (red dash line) for the E-plane (xz-plane) patterns.

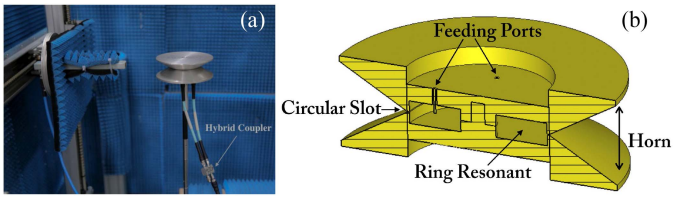

Fig. 8. (a) An antenna prototype for generation of PS-OAM waves of $l = \pm 3$ with two feeding ports, and (b) schematic of ring horn loaded traveling-wave circular slot antenna.

$J_l(\cdot)$, the radiation direction of different modes are all toward to $\theta = 90°$. The ring dielectric resonator antenna is proposed to generate PS-OAM as shown in Fig. 6 [14]. Fig. 7(a) shows the simulated 3D radiation pattern. The generated wave propagates mainly along the transverse plane. Fig. 7(b) shows the simulated and measured 2D far-field radiation patterns in the transverse plane.

The second method is to load the ring horn [8], [15]. A prototype with OAM states $l = \pm 3$ for 10 GHz operation is shown in Fig. 8(a), while Fig. 8(b) presents the internal structure of the fabricated antenna. The simulated and measured far-field patterns are shown in Fig. 9.

The third method is to load a rotating parabolic reflector (RPR) [16]. As shown in Fig. 10(a), the proposed antenna consists of a coaxial resonator group (CRG) and an RPR. The CRG consists of four top-slotted TE coaxial resonators sequentially arranged from inside to outside, which is displayed intuitively in its cross-section view in Fig. 10(b). The nth resonator works in TE_{n11} standing-wave mode and has two feeding ports, which are fed by a 90° hybrid coupler. According to Euler's formula, the traveling-wave mode could be generated in the resonator, and

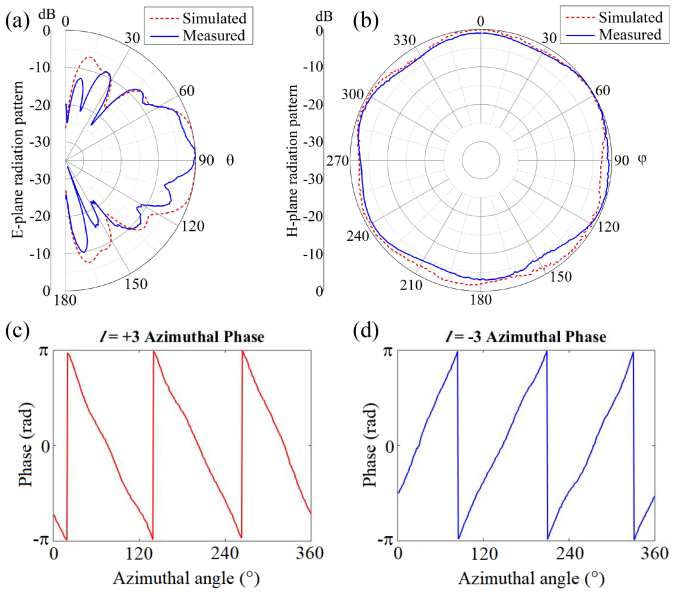

Fig. 9. Far-field radiation of ring horn loaded traveling-wave circular slot antenna for $l = \pm 3$. (a) E-plane radiation pattern, (b) H-plane radiation pattern, (c) and (d) Phase distributions with azimuthal angle.

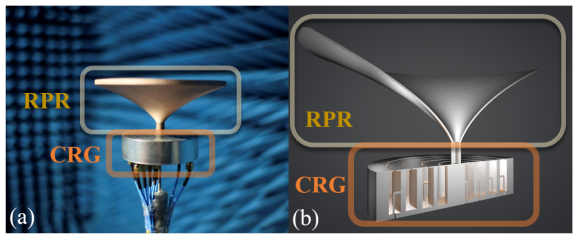

Fig. 10. Antenna design: (a) antenna prototype; (b) cross-section view of the antenna model.

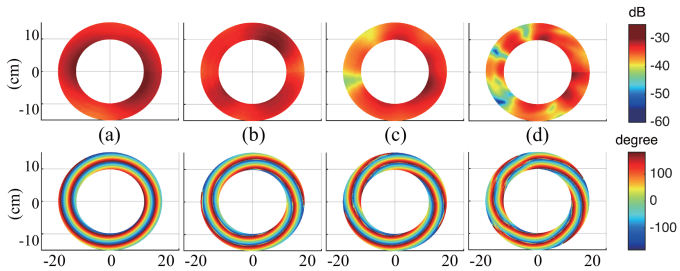

Fig. 11. Near-field power and phase distribution of single mode at xoy plane: (a) mode $l = 1$; (b) mode $l = 2$; (c) mode $l = 3$; (d) mode $l = 4$.

the OAM wave of mode l_n is radiated from the slot. Similarly, the OAM wave of mode $-l_n$ could be radiated when the iso-port is fed. Hence the OAM waves of mode $l = \pm 1, \pm 2, \pm 3, \pm 4$ can be generated and controlled independently. The RPR converts OAM waves to PS-OAM waves by reflecting them to the horizontal plane according to the principle of geometrical optics. Its surface satisfies parabolic equation $Z = \sqrt{2 \times P \times \rho}$, where P is the parabola focal length.

Fig. 11 shows each mode's near-field power and phase distribution at the E-plane, respectively. It is seen that the PS-OAM

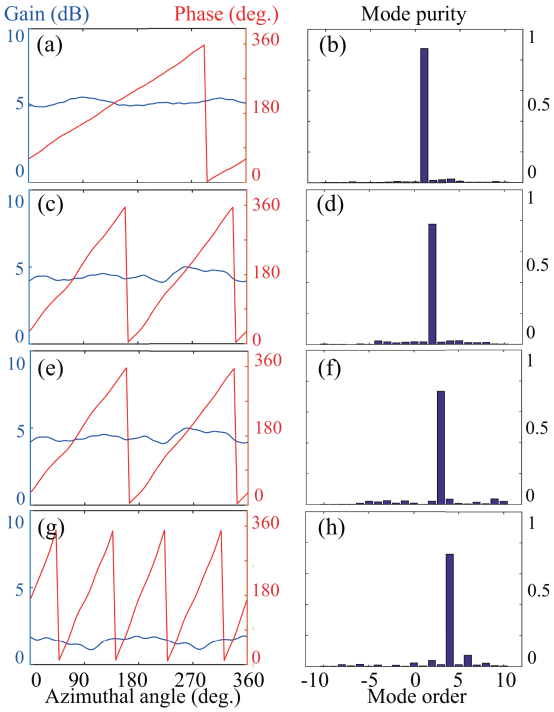

Fig. 12. Far-field gain, phase distributions and mode purity of the PS-OAM modes at the H-plane (θ =90°): (a) gain and phase distributions of mode $l = 1$; (b) mode purity of mode $l = 1$; (c) gain and phase distributions of mode $l = 2$; (d) mode purity of mode $l = 2$; (e) gain and phase distributions of mode $l = 3$; (f) mode purity of mode $l = 3$; (g) gain and phase distributions of mode $l = 4$; (h) mode purity of mode $l = 4$.

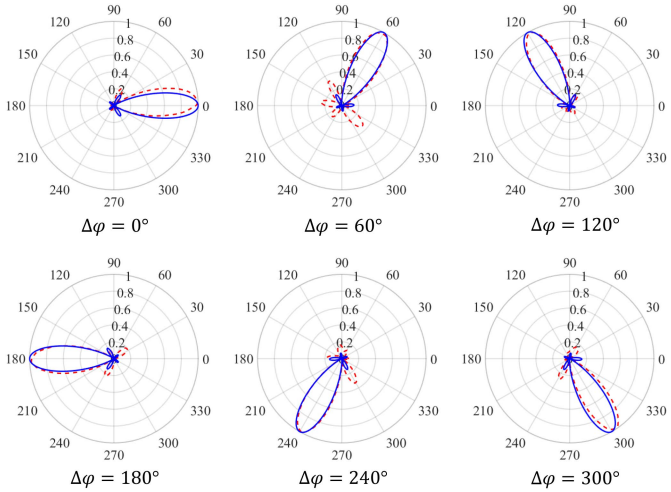

Fig. 13. Normalized theoretical (blue line) and measured (red line) patterns of the pencil beams constructed by eight modes.

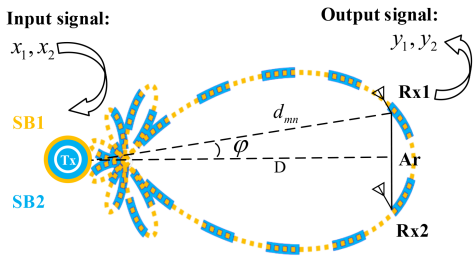

Fig. 14. System configuration of such MIMO system. d_{mn}: the propagation distance between the mth SB and the nth Rx.

beams have good phase linearity and amplitude uniformity in the azimuthal domain in the near-field region.

Fig. 12(a),(c),(e),(g) present the far-field gain and phase distribution of each mode at the E-plane, respectively. In the near-field region, the wave keeps stable vortex phase distribution and relatively uniform energy distribution. Based on the far-field distribution, the OAM mode purity of each resonator is illustrated in Fig. 12(b),(d),(f),(h), respectively. It can be seen that all the generated PS-OAM waves have high mode purity, which is of great significance for the structured radio beams.

With the designed antenna, eight PS-OAM modes can be generated and controlled independently. A feeding network composed of attenuators and phase shifters is cascaded before the input ports (including in-port and iso-port) for weighting all PS-OAM waves. Hence, this antenna can be used to realize the structured radio beams. Any azimuthal target pattern can be reconfigured by calculating the complex OAM mode purity and feeding the corresponding amplitude and phase to the mode.

As described in Section II, a pencil beam can be constructed by multiple OAM beams with consecutive modes of equal amplitude and the same phase. Fig. 13 shows the pencil beams built by all eight modes with the different phase difference between adjacent modes $\Delta\varphi$. It is seen that the main lobe direction is dependent on $\Delta\varphi$. The PS-OAM based beam scanning has the ability of omnidirectional 360° scanning without distortion in the azimuthal domain as expected [17].

IV. Potential Applications

A. MIMO System

The structured radio beam can be applied to the transmitting end in an LoS-MIMO system [11], [18]. The common high gain beams used in MIMO systems just improve the signal-to-noise ratio (SNR), and the differences among channels are simply caused by different propagation paths. Whereas the structured beams cannot only improve the SNR, but also decrease the spatial correlations between sub-channels which benefits from the abundant phase information.

The proposed MIMO system is shown in Fig. 14. The model is illustrated as a 2×2 LoS-MIMO system. At the transmitting end, the antennas for structured beams (SBs) are placed coaxially and then radiate into the free space from the same point. At the receiving end, two general horn antennas are placed at the symmetry positions along the propagation axis. Focusing on the link performance, several considerations are assumed,

- The number of the structured beams equals the number of horn antennas.
- By contrast, the transmitting aperture of the existing MIMO system is $l_{\max}\lambda/\pi$, where $l_{\max}$ is the highest order OAM mode among the structured beams.

The channel model of the proposed system could be expressed as a narrow-band MIMO system, which is as follows [19],

$$\mathbf{y} = \mathbf{H}_{\mathrm{SB}}\mathbf{x} + \mathbf{n} \tag{5}$$

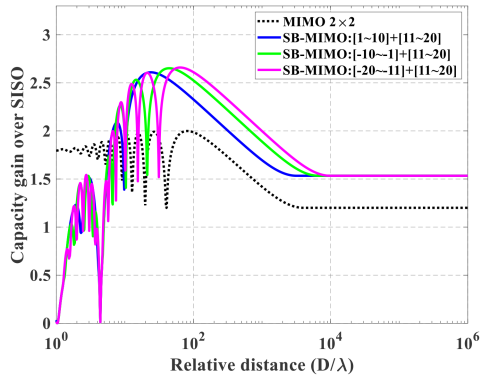

Fig. 15. Capacity gain over SISO system for existing MIMO system, PSOAM-MIMO system and SB-MIMO system. The receiving SNR is 30 dB and the Rayleigh distance of $2A_r^2/\lambda$ is approximately 82λ.

where $\mathbf{H}_{\mathrm{SB}} \in \mathbb{C}^{2\times 2}$ is the transfer matrix consisted of several transfer functions. The performance of channel capacity can be analyzed utilizing singular value decomposition (SVD) algorithm [19].

Fig. 15 presents the capacity gain of the existing MIMO system and structured beam based MIMO system (SB-MIMO or MG-MIMO) in an LoS scenario [11]. The multiplexed SBs are SB^{a} $\{1, 2, \ldots, 9, 10\}$, SB^{b} $\{11, 12, \ldots, 19, 20\}$, SB^{c} $\{-10, -9, \ldots, -2, -1\}$, and SB^{d} $\{-20, -19, \ldots, -12, -11\}$. Each SB has the same certain intensity pattern. The capacity gains are simulated numerically at a receiving SNR of 30 dB no matter how long the relative distance D is.

Benefitting from the SNR improvement due to the directionality of the structured beam, the proposed scheme has a better peak gain about 2.6. Besides, to achieve the same capacity gain such as 2, the proposed scheme can propagate much longer, e.g., multiplexed SBs are SB^{a} and SB^{b} (blue line), the propagating distance is raised from 84λ of MIMO system to 328λ. Interestingly, for the same receiving aperture and same mainlobe gain, if the difference value of equivalent OAM mode order Δl_e between multiplexed SBs is larger, the correlation of sub-channels is going to be lower.

We set up a 2×2 MG-MIMO prototype to demonstrate and verify the impact on communication performance of the vorticity of structured beams [20]. Here, the sub-channel difference is merely brought by the linear phase distribution of the structured beams. At the receiving end, two horn antennas spaced 0.6 cm apart are placed at the symmetry positions along the propagation axis, as illustrated in Fig. 16(a). The communication distance D is 5 m. Four pairs of MGs used for conducting the comparison experiments are $\mathrm{MG}^1\{-1, 1\}$ and $\mathrm{MG}^2\{-2, 2\}$ with Δl_e of 0 (a pair of plane waves) [17], $\mathrm{MG}^3\{1, 2\}$ and $\mathrm{MG}^4\{-2, -1\}$ with Δl_e of 3, $\mathrm{MG}^5\{2, 3\}$ and $\mathrm{MG}^6\{-3, -2\}$ with Δl_e of 5, $\mathrm{MG}^7\{3, 4\}$ and $\mathrm{MG}^8\{-4, -3\}$ with Δl_e of 7, respectively.

The measured raw BER curves of the QPSK transmission and the 16-QAM transmission have been shown in Fig. 16(b) and 16(c), respectively. For both two modulation formats, as Δl_e increases from 0 to 3, 5, and 7, the corresponding BER value is reduced to some extent, i.e., the communication performance is getting better for the case of larger Δl_e. It's worth noting

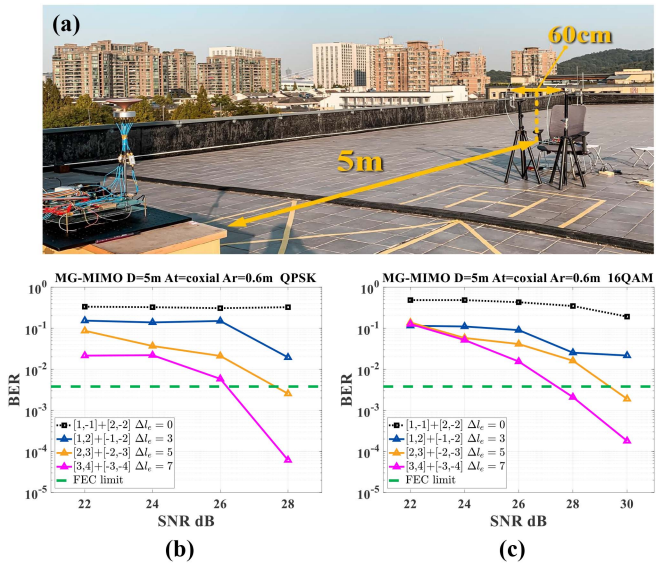

Fig. 16. (a) Experimental setup used to study the impact on communication link performance of MG's vorticity. (b) The QPSK transmission: the measured raw BER performance for these four pairs of multiplexed MGs. (c) The 16-QAM transmission: the measured BER.

that the difference of sub-channels is entirely caused by the MG's vorticity rather than the propagation path difference, as the MIMO system does. Owing to the coaxial arraying way at the transmitting end, for the receiving horns arranged symmetrically along the propagation axis, the wave-path of two plane waves to the two receiving antennas are almost the same, which means that there is no spatial diversity between the multiplexed signals. Hence, the system cannot support the multiplexing, and severe aliasing occurs between the multiplexed signals, the BER values at each SNR for both modulation formats are all above the level of 20%. It's an intolerable level in wireless communication.

For the QPSK transmission, as far as the test results are concerned, when Δl_e is 5 or 7, the MG-MIMO system can reach the FEC limit of 3.8×10^{-3}. Thanks to the lower sub-channel correlation, the multiplexing of MG^7 and MG^8 can reach the such limit at a lower SNR of about 26 dB, and the multiplexing of MG^5 and MG^6 needs a 28 dB SNR to reach the same limit. As for the 16-QAM transmission, similarly, when Δl_e is 5 or 7, the MG-MIMO system can reach the FEC limit. The multiplexing case of $\Delta l_e = 7$ reaches the FEC limit at a lower SNR of about 28 dB, and the multiplexing case of $\Delta l_e = 5$ requires a higher SNR of 30 dB to reach this limit.

In addition, it has also been verified experimentally that the BER and robustness performance of the proposed MG-MIMO outperforms conventional MIMO [20], which benefits from MG's directionality and vorticity. In [21], it has been evaluated that MG-MIMO has potential in long-distance point-to-point wireless transmission scenarios through contrastive analysis.

B. *Orthogonal Multiplexing Communication*

Structured radio beam as a reconfigurable beamforming method can be used to build a MIMO system to reduce sub-channel correlation. However, the demultiplexing process still

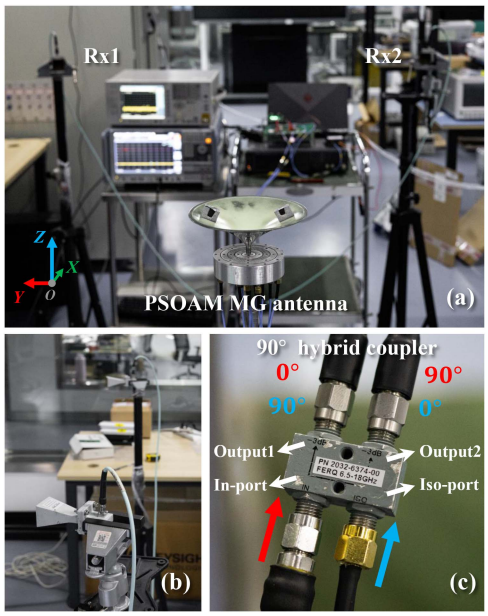

Fig. 17. (a) Experimental setup of the communication link. (b) The receiving end adopts the standard gain horn antennas, they are placed symmetrically on both sides of the propagation axis. (c) A 90° hybrid coupler can be used for demultiplexing the signals based on PASR scheme.

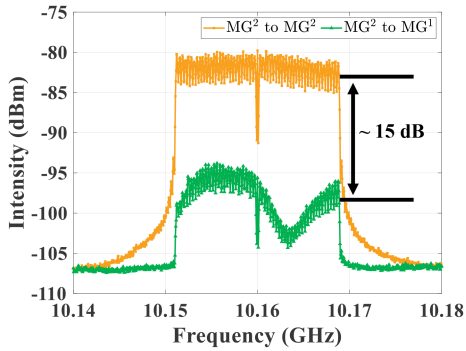

Fig. 18. The channel isolation between multiplexed PSOAM MGs over the entire working band.

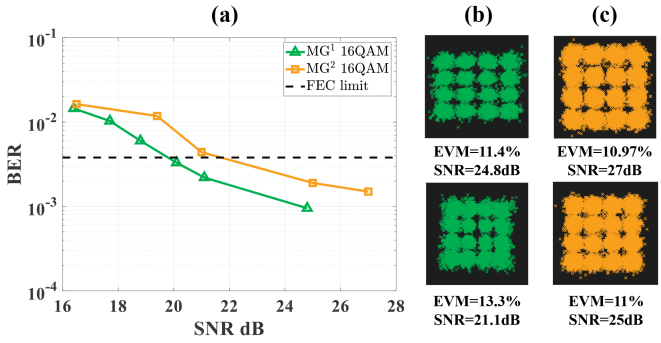

Fig. 19. (a) Measured BER performances of the 16-QAM multiplexing. (b) The typical constellations with EVM performance from MG^1 channel at the corresponding SNR. (c) The typical constellations with EVM performance from MG^2 channel.

depends on the MIMO algorithm, where the receiver complexity is the same as conventional MIMO systems. Because of its main-lobe's spiral phase distribution similar to conventional OAM wave, structured radio beam also possesses the orthogonality under partial arc sampling receiving (PASR) scheme [17], [22]. It is worth noticing that the demultiplexing process can be completely realized by a simple analog phase shifting operation, and the receiver complexity can be reduced significantly.

On the basis of PASR scheme [23], for $2\pi/\delta$ azimuthal arc and N_r receiving antennas, the angle difference between neighbouring antennas meets $2\pi/(\delta N_r)$. If $\Delta l_e^{12} = l_e^1 - l_e^2$ is equal to $k'\delta$, where k' is a non-zero integer, the multiplexed MG^1 and MG^2 can be demultiplexed orthogonally.

A PS-OAM mode-group (PSOAM MG) orthogonal multiplexing communication link at X-band using the PASR scheme has been demonstrated experimentally [24]. Fig. 17(a) shows the experimental setup in an LoS scenario. A pair of MGs used for conducting the experiments are $\mathrm{MG}^1\{1, 2, 3, 4\}$ with l_e^1 of 2.5 and $\mathrm{MG}^2\{-1, -2, -3, -4\}$ with l_e^2 of -2.5, Δl_e^{12} is equal to 5. The communication distance is set as 2 m; based on the PASR scheme, the receiving aperture A_r needs to be set as 1.29 m. The receiving end adopts the standard gain horn antennas to form the uniform linear array, which guarantees that they could be placed symmetrically along the propagation axis, as shown in Fig. 17(b). According to PASR scheme [22], for this case, a group of phase shifts should be set as 0° at Rx1 and 90° at Rx2 to demultiplex MG^1. Meanwhile, the other group should be set as 90° at Rx1 and 0° at Rx2 to demultiplex MG^2. A 90° hybrid coupler is used for synchronously realizing such analog phase shift operation, as shown in Fig. 17(c).

First, the channel isolation between two PSOAM MGs is tested over the entire working band. At the transmitting end, we only feed the bandpass signal into MG^2 while MG^1 is disabled, then the spectrum of receiving signals is obtained from the corresponding channels. As shown in Fig. 18, the power level of MG^2 channel is $\sim$15 dB higher than that of MG^1 channel. The channel isolation between multiplexed MGs under the PASR scheme can maintain the level of about 15 dB, which means that two independent wireless channels have been established under existing conditions.

Then, the multiplexing communication experiment is carried out. At the transmitting end, two 16-QAM signals carrying different data streams are fed simultaneously to MG^1 channel and MG^2 channel, respectively. As shown in Fig. 19(a), the BER curves of two channels can reach the FEC limit, which proves the validity of multiplexing communication. Besides, Fig. 19(b) and (c) show the typical constellations with EVM performance. The measured EVM values from MG^1 channel are 11.4% and 13.3% at the SNR of 24.8 dB and 21.1 dB, respectively. Moreover, for MG^2 channel, its EVM performances are 10.97% and 11% at the SNR of 27 dB and 25 dB, respectively.

Moreover, the comparison of this work with other analog spatial multiplexing transmission systems has been shown and discussed detailedly in [24]. In terms of measured channel isolation, single-way spectrum efficiency, and total spectrum efficiency, the performances of our system are relatively good. The next step is to further improve system bandwidth and data rate.

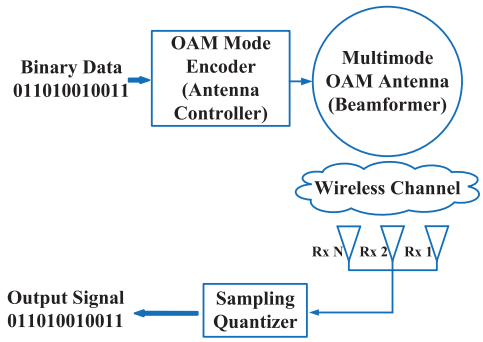

Fig. 20. The architecture of the OAM-SFDM system.

C. Spatial Field Digital Modulation

To pursue higher spectral and energy efficiency, a type of new modulation scheme, index modulation (IM) has been proposed and studied [25]. There are various of IM schemes directly modulating information in the spatial distribution of the electromagnetic field, including space shift keying [26], media-based modulation [27], channel modulation [28], directly digital modulation [29], and spatially encoded data transmission [30]. The key to realizing these modulation schemes is to radiate different electromagnetic fields, i.e., different far-field patterns.

The PS-OAM based beamforming is a flexible method to control both the amplitude and the phase distributions of the electromagnetic field, and provides the azimuthal pattern diversity. Thus, a PS-OAM based spatial field digital modulation (OAM-SFDM) system is proposed [31] [32] to realize the aforementioned IM scheme.

Fig. 20 shows the architecture of the OAM-SFDM system. The transmitted binary data is truncated into k-bit fragments. Each bit fragment is mapped to a symbol, and is input to the OAM mode encoder. In the OAM mode encoder, the combinations of the amplitude and the initial spatial phase of each OAM mode are determined. Then, the multimode OAM antenna is controlled to transmit the SFDM signal, i.e., the EM field with a specific amplitude and phase distribution. In the receiving end, the receiver array measures the EM field at several points in the spatial dimension and outputs the results to the sampling quantizer. According to a predefined demodulation criterion, the sampling quantizer estimates the transmitted symbol from the received signal, and recovers the original information.

Different demodulation methods with different performance and complexity can be chosen to demodulate the SFDM signal. In [31], a maximum likelihood (ML) detector based on the Euclidean distance is adopted. The ML detector requires the phase difference between the transmitter and the receiver, which is usually impractical. To develop an alternative demodulation method that can work without requirement for the phase difference, the spatial matched filtering criterion is proposed to demodulate the SFDM signal [32].

A proof-of-principle experiment is carried out to verify the validity of the spatial matched filtering criterion [32]. Fig. 21(a) is the schematic diagram of the SFDM system architecture. In

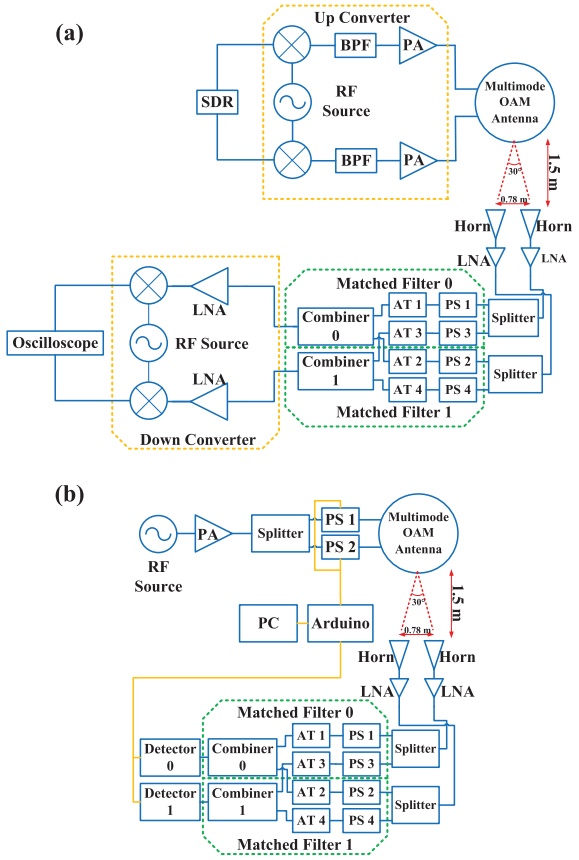

Fig. 21. The schematic diagram of the SFDM system architecture in this experiment with 1.5 m communication distance, in which the transmitting antenna operates at 10.16 GHz. SDR: software defined radio, BPF: band-pass filter, LNA: low-noise amplifier, PA: power amplifier, PS: electrically-tuned phase shifter, AT: electrically-tuned attenuator, Detector: logarithmic RMS power detector. (a) The high-speed SFDM system. (b) The low-complexity SFDM system.

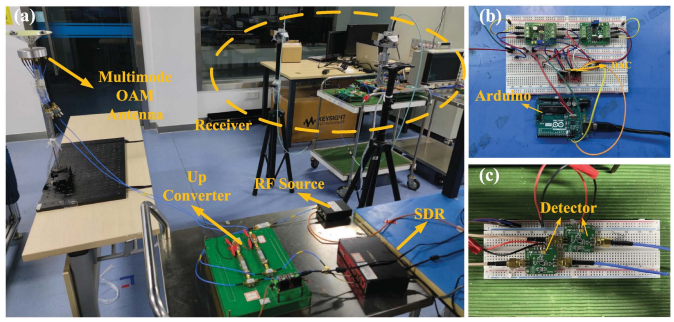

Fig. 22. (a) The photo of the implemented high-speed SFDM system. (b) The antenna controller of the low-complexity SFDM system. (c) The detectors of the low-complexity SFDM system.

this experiment, the bit rate is about 92 kbit/s. Moreover, an alternative low-complexity SFDM scheme is shown in Fig. 21(b). In this alternative scheme, the phase difference of the signals fed into the OAM antenna is controlled by the electrically tuned phase shifters, and the output powers of the filters are measured by the logarithmic RMS power detectors. This low-complexity SFDM system has a lower cost than the original one, but its bit rate is lower as well, which is about 400 bit/s. Fig. 22

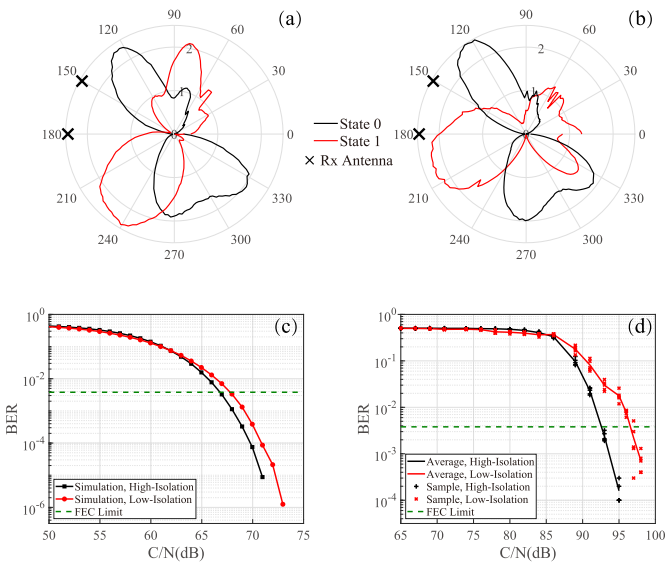

Fig. 23. (a) The far-field patterns of two selected states in the high-isolation scheme. (b) The far-field patterns of two selected states in the low-isolation scheme. (c) The simulated BER performances of the high-isolation and the low-isolation scheme. (d) The experimental BER performances of the highisolation and the low-isolation schemes. The BER measurements are carried out for 5 times at each C/N, and the results are marked with two different crosses. The black and the red solid lines are plotted from the average of the measurement results at each C/N.

are the photos of the two implemented SFDM systems. The communication distance of each SFDM system is 1.5 m.

Fig. 23 are the numerical simulation and the experiment results of the low-complexity SFDM system. The far-field patterns carrying the information are shown in Fig. 23(a), (a). In this experiment, two different modulation schemes having different state isolations are designed. The state isolation is defined as the difference of the output powers between the Filter 0's and Filter 1's at the same state. Since a more significant difference between the output power of the "matched filter" and those of the "mismatched filters" can lead to a lower BER and a stronger anti-noise ability, the high-isolation scheme is expected to have a better BER performance. The results of the numerical simulation and the experiment both support the hypothesis. The figure indicates that the low-complexity SFDM system can also realize error-free transmission.

V. Conclusion

We extend the concept of structured light to radio-frequency electromagnetic wave. The complex spatial phase and amplitude distribution in a specific beam can be constructed by grouping OAM mode waves in space. This novel kind of beam inherits the inherent vorticity and orthogonality of OAM wave, and has three advantages. Its amplitude directional gain can improve the signal-to-noise ratio of communication link. The phase vortex characteristic can enrich the difference between subchannels in MIMO system. The quasi orthogonal property between beams can simplify the signal processing at the receiving end. Therefore, spatial structured radio beam is expected to overcome the problems of traditional OAM beam and expand the applications of OAM characteristics in communications.

References

[1] L. Allen, M. W. Beijersbergen, R. J. C. Spreeuw, and J. P. Woerdman, "Orbital angular momentum of light and the transformation of Laguerre-Gaussian laser modes," *Phys. Rev. A*, vol. 45, pp. 8185–8189, Jun. 1992.

[2] M. Padgett, "Orbital angular momentum 25 years on," *Opt. Exp.*, vol. 25, 2017, Art. no. 11265.

[3] B. Thidé et al., "Utilization of photon orbital angular momentum in the low-frequency radio domain," *Phys. Rev. Lett.*, vol. 99, Aug. 2007, Art. no. 0 87701.

[4] S. M. Mohammadi, L. K. S. Daldorff, J. E. S. Bergman, R. L. Karlsson, and T. D. Carozzi, "Orbital angular momentum in radio–A system study," *IEEE Trans. Antennas Propag.*, vol. 58, no. 2, pp. 565–572, Feb. 2010.

[5] H. Rubinsztein-Dunlop et al., "Roadmap on structured light," *J. Opt.*, vol. 19, no. 1, Nov. 2017, Art. no. 013001.

[6] M. J. Padgett, F. M. Miatto, M. P. J. Lavery, A. Zeilinger, and R. W. Boyd, "Divergence of an orbital-angular-momentum-carrying beam upon propagation," *New J. Phys.*, vol. 17, no. 2, Feb. 2015, Art. no. 0 23011.

[7] S. Zheng, Z. Zhang, Y. Pan, X. Jin, H. Chi, and X. Zhang, "Plane spiral orbital angular momentum electromagnetic wave," in *Proc. Asia-Pacific Microw. Conf.*, vol. 3, 2015, pp. 1–3.

[8] Z. Zhang, S. Zheng, J. Zheng, X. Jin, H. Chi, and X. Zhang, "Plane spiral orbital angular momentum wave and its applications," in *Proc. IEEE MTT-S Int. Microw. Symp.*, 2016, pp. 1–4.

[9] X. Zhang and S. Zheng, "Grouping plane spiral electromagnetic waves for structured RF beams," in *Proc. Sixth Asia-Pacific Conf. Antennas Propag.*, 2017, pp. 1–3.

[10] Z. Wang et al., "Structure radio beam construction in azimuthal domain," *IEEE Access*, vol. 8, pp. 9395–9402, 2020.

[11] X. Xiong, S. Zheng, Z. Zhu, X. Yu, X. Jin, and X. Zhang, "Performance analysis of plane spiral OAM mode-group based MIMO system," *IEEE Commun. Lett.*, vol. 24, no. 7, pp. 1414–1418, Jul. 2020.

[12] S. Zheng, X. Hui, X. Jin, H. Chi, and X. Zhang, "Transmission characteristics of a twisted radio wave based on circular traveling-wave antenna," *IEEE Trans. Antennas Propag.*, vol. 63, no. 4, pp. 1530–1536, Apr. 2015.

[13] X. Hui et al., "Multiplexed millimeter wave communication with dual orbital angular momentum (OAM) mode antennas," *Sci. Rep.*, vol. 5, 2015, Art. no. 10148.

[14] R. Dong et al., "Generation of plane spiral orbital angular momentum microwave with ring dielectric resonator antenna," in *Proc. 6th Asia-Pacific Conf. Antennas Propag.*, 2017, pp. 1–3.

[15] Z. Zhang, S. Zheng, X. Jin, H. Chi, and X. Zhang, "Generation of plane spiral OAM waves using traveling-wave circular slot antenna," *IEEE Antennas Wireless Propag. Lett.*, vol. 16, pp. 8–11, 2017.

[16] Z. Zhu et al., "A compact pattern reconfiguration antenna based on multimode plane spiral OAM," *IEEE Trans. Antennas Propog.*, vol. 69, no. 2, pp. 1168–1172, Feb. 2021.

[17] S. Zheng et al., "Realization of beam steering based on plane spiral orbital angular momentum wave," *IEEE Trans. Antennas Propag.*, vol. 66, no. 3, pp. 1352–1358, Mar. 2018.

[18] X. Xiong et al., "Direct generation of OAM mode-group and its application in LoS-MIMO system," *IEEE Commun. Lett.*, vol. 24, no. 11, pp. 2628–2631, Nov. 2020.

[19] O. Edfors and A. J. Johansson, "Is orbital angular momentum (OAM) based radio communication an unexploited area?," *IEEE Trans. Antennas Propag.*, vol. 60, no. 2, pp. 1126–1131, Feb. 2011.

[20] X. Xiong et al., "Experimental study of plane spiral OAM mode-group based MIMO communications," *IEEE Trans. Antennas Propag.*, vol. 70, no. 1, pp. 641–653, Jan. 2022.

[21] X. Xiong et al., "Long-range mimo communication using plane spiral oam mode-group," in *Proc. IEEE MTT-S Int. Wireless Symp.*, 2021, pp. 1–3.

[22] W. Zhang, S. Zheng, Y. Chen, X. Jin, H. Chi, and X. Zhang, "Orbital angular momentum-based communications with partial arc sampling receiving," *IEEE Commun. Lett.*, vol. 20, no. 7, pp. 1381–1384, Jul. 2016.

[23] S. Zheng et al., "Orbital angular momentum mode-demultiplexing scheme with partial angular receiving aperture," *Opt. Exp.*, vol. 23, no. 9, pp. 12251–12257, Apr. 2015.

[24] X. Xiong et al., "Plane spiral OAM mode-group orthogonal multiplexing communication using partial arc sampling receiving scheme," *IEEE Trans. Antennas Propag.*, early access, Jul. 12, 2022, doi: 10.1109/TAP.2022.3188386., .

[25] E. Basar, M. Wen, R. Mesleh, M. Di Renzo, Y. Xiao, and H. Haas, "Index modulation techniques for next-generation wireless networks," *IEEE Access*, vol. 5, pp. 16693–16746, 2017.
[26] J. Jeganathan, A. Ghrayeb, L. Szczecinski, and A. Ceron, "Space shift keying modulation for MIMO channels," *IEEE Trans. Wireless Commun.*, vol. 8, no. 7, pp. 3692–3703, Jul. 2009.
[27] A. K. Khandani, "Media-based modulation: A new approach to wireless transmission," in *Proc. IEEE Int. Symp. Inf. Theory*, 2013, pp. 3050–3054.
[28] E. Basar and I. Altunbas, "Space-time channel modulation," *IEEE Trans. Veh. Technol.*, vol. 66, no. 8, pp. 7609–7614, Aug. 2017.
[29] T. J. Cui, S. Liu, G. D. Bai, and Q. Ma, "Direct transmission of digital message via programmable coding metasurface," *Research*, vol. 2019, 2019, Art. no. 2584509.
[30] A. Chepala, Y. Ding, and V. F. Fusco, "Multimode circular antenna array for spatially encoded data transmission," *IEEE Trans. Antennas Propag.*, vol. 67, no. 6, pp. 3863–3868, Jun. 2019.
[31] Y. Chen, X. Xiong, Z. Zhu, S. Zheng, and X. Zhang, "Orbital angular momentum mode-group based spatial field digital modulation: Coding scheme and performance analysis," in *Proc. IEEE Int. Conf. Commun. Workshops*, 2020, pp. 1–4.
[32] Y. Chen et al., "Experimental demonstration of OAM spatial field digital modulation communication system," *IEEE Commun. Lett.*, vol. 26, no. 10, pp. 2470–2474, Oct. 2022.

Xianmin Zhang received the B.S. and Ph.D. degrees in physical electronics and optoelectronics from Zhejiang University, Hangzhou, China, in 1987 and 1992, respectively. He was appointed as an Associate Professor of information and electronic engineering with Zhejiang University in 1994 and a Full Professor in 1999. He was a Research Fellow with the University of Tokyo, Tokyo, Japan, and Hokkaido University, Sapporo, Japan, from November 1996 to September 1997, and October 1997 to September 1998, respectively. In 2007, he spent two months with the Research Laboratory of Electronics, Massachusetts Institute of Technology, Cambridge, MA, USA, as a Visiting Research Fellow. He was the Dean of the Department of Information Science and Electronic Engineering, Zhejiang University, from September 2005 to November 2017, the Dean of the School of Microelectronics, Zhejiang University, from May 2015 to September 2018, the Vice Dean of Polytechnic Institute, Zhejiang University, from July 2016 to September 2018, the President of the Ningbo Institute of Technology, Zhejiang University, from July 2018 to April 2020, and the Dean of Ningbo Campus, Zhejiang University, from September 2018 to November 2020. He is currently the Vice President of NingboTech University, Ningbo, China. His research interests include microwave photonics, electromagnetic wave theory and applications.

Shilie Zheng (Member, IEEE) received the B.S. and the M.S. degrees in materials science and the Ph.D. degree in physical electronics and optoelectronics from Zhejiang University, Hangzhou, China, in 1995, 1998, and 2003, respectively. In 1998, she joined the Department of Information Science and Electronic Engineering, Zhejiang University, where she was appointed as an Associate Professor in 2005. From November 2005 to March 2006, she spent five months at Tohoku University, Sendai, Japan as a Research Assistant. From July 2016 to July 2017, she was a Visiting Research Fellow with RF and Microwave Laboratory, National University of Singapore, Singapore. At the end of 2017, she was appointed as a Full Professor with Zhejiang University. Her research interests include twisted radio waves and applications, microwave photonics and wireless communications.

Xiaowen Xiong (Member, IEEE) received the B.S. degree in communication engineering from the Nanjing University of Posts and Telecommunications, Nanjing, China, in 2017, and the Ph.D. degree in electronic science and technology from Zhejiang University, Hangzhou, China, in 2022. In 2022, he joined the Department of Electronic Engineering, Tsinghua University, Beijing, China, as a Postdoctoral Research Fellow. His research interests include RF and microwave system, wireless communication, antenna, OAM wave and its applications. He was the recipient of the Best Student Paper Honorable Mention in the 2021 IEEE MTT-S International Wireless Symposium (IWS 2021). He also was the Reviewer for IEEE TRANSACTIONS ON ANTENNAS AND PROPAGATION, IEEE COMMUNICATIONS LETTERS and IEEE WIRELESS COMMUNICATIONS LETTERS.

Zelin Zhu received the B.S. degree in electronic information science and technology from the University of Electronic Science and Technology of China, Chengdu, China, in 2018. He is currently working toward the Ph.D. degree in electronic science and technology with Zhejiang University, Hangzhou, China. His research interests include vortex electromagnetic wave antenna and its applications in radar system and communication system.

Yuqi Chen (Graduate Student Member, IEEE) received the B.S. degree from the University of Electronic Science and Technology of China, Chengdu, China, in 2019. He is currently working toward the Ph.D. degree in electronic science and technology with Zhejiang University, Hangzhou, China. His research interests include orbital angular momentum antenna and its applications in wireless communication.

Zhixia Wang received the B.S. degree in communication engineering from the Zhejiang University of Technology, Hangzhou, China, in 2018. She is currently working toward the Ph.D. degree in electronic science and technology with Zhejiang University, Hangzhou, China. Her research interests include twisted radio waves, terahertz orbital angular momentum and its application in wireless communications.

Xiaonan Hui received the B.S. degree in electrical engineering from Northeastern University, Shenyang, China, in 2012, the M.S. degree from Zhejiang University, Hangzhou, China, in 2015, and the Ph.D. degree in electrical engineering from Cornell University, Ithaca, NY, USA, in 2021. In 2021, he joined the College of Information Science and Electronic Engineering, Zhejiang University as an Assistant Professor. His research interests include wireless sensing, RFID, IoT, and wireless communication systems.

Wei E. I. Sha (Senior Member, IEEE) received the B.S. and Ph.D. degrees in electronic engineering from Anhui University, Hefei, China, in 2003 and 2008, respectively. From July 2008 to July 2017, he was a Postdoctoral Research Fellow and then a Research Assistant Professor with the Department of Electrical and Electronic Engineering, University of Hong Kong, Hong Kong. From March 2018 to March 2019, he was with University College London, London, U.K., as a Marie-Curie Individual Fellow. In October 2017, he joined the College of Information Science & Electronic Engineering, Zhejiang University, Hangzhou, China, where he is currently a tenure-tracked Assistant Professor. His research interests include theoretical and computational research in electromagnetics and optics, focusing on the multiphysics and interdisciplinary research, fundamental and applied aspects in computational and applied electromagnetics, nonlinear and quantum electromagnetics, micro- nano-optics, optoelectronic device simulation, and multiphysics modeling.

Xianbin Yu (Senior Member, IEEE) is currently a Professor with Zhejiang University, Hangzhou, China. He has given more than 40 invited talks in prestigious international conferences within the area of optical communications and RF photonics technologies, and has coauthored three book chapters and more than 200 peer-reviewed international journal and conference papers. His research interests include ultrafast millimeter-wave/THz photonic information processing, ultrahigh frequency photonic wireless communication systems, and also emerging new applications of millimeter-wave/THz technologies. He was the Session Chair/TPC Member for a number of international conferences.